International Journal of Heat and Mass Transfer 219 (2024) 124878

Contents lists available at ScienceDirect

International Journal of Heat and Mass Transfer

journal homepage: www.elsevier.com/locate/ijhmt

Three-sensor 2ω method with multi-directional layout: A general methodology for measuring thermal conductivity of solid materials

Guang Yang, Bing-Yang Cao *

Key Laboratory for Thermal Science and Power Engineering of Ministry of Education, Department of Engineering Mechanics, Tsinghua University, Beijing 100084, China

ARTICLE INFO

Keywords:
Anisotropic thermal conductivity
2ω method
Three-sensor layout
Thermal conductivity measurement

ABSTRACT

Anisotropic thermal transport plays a key role in both theoretical study and engineering practice of heat transfer, but accurately measuring anisotropic thermal conductivity remains a significant challenge. To address this issue, we propose the three-sensor 2ω method in this study, which is capable of accurately measuring the isotropic or anisotropic thermal conductivity of solid materials. In this method, several three-sensor groups following the design guidelines are fabricated upon the sample along different characteristic directions, and each group consists of three parallel metal sensors with unequal widths and distances optimally designed based on sensitivity analysis. Among the three sensors, the outer two serve as AC heaters and the middle one as a DC detector. The 2ω voltage signals across the detector in each three-sensor group are measured, and then the data are processed by the proposed Intersection Method to derive thermal conductivities along directions of interest. The application of the detector's 2ω instead of the heater's 3ω voltage signals eliminates errors introduced by the uncertainties of thermal resistance in superficial structures (metal layer, insulation layer, interface, etc.). Meanwhile, by replacing the fitting algorithm with the Intersection Method, the local optimum trap of multivariate fitting is avoided. To verify the accuracy and reliability, four typical monocrystalline semiconductors, i.e., Si, GaN, AlN, and β-Ga_2O_3, are measured, and the results are consistent with the literature. This method will provide a comprehensive and versatile solution for the thermal conductivity measurements of solid materials.

1. Introduction

Anisotropic heat transport phenomena are ubiquitous in materials, and are crucial to the theoretical study and technological development of heat transfer [1]. On the one hand, if the lattice structure of a material is highly asymmetric, it generally exhibits a significant anisotropic thermal conductivity. On the other hand, if a material with a symmetric lattice contains highly oriented lattice defects (e.g., dislocations, grain boundaries, stacking faults), it tends to exhibit an anisotropic thermal conductivity likewise [2,3]. For various advanced technology fields, anisotropic thermal conductivity is one of the key indicators that determine the performance and reliability, especially in the thermal management of electronic devices [4], thermal rectification [5], high-temperature superconductor [6], thermal photovoltaics [7,8], and thermoelectricity [9,10], etc. In recent years, researchers have made considerable progress in developing experimental techniques for thermal conductivity measurement, however, accurately measuring the anisotropic thermal conductivity of solid materials remains a challenge.

The experimental techniques available for measuring the anisotropic thermal conductivity of solid materials include two categories: optical and electrical methods. The optical methods mainly include the ultrafast laser transient thermoreflectance (TTR, including the original time-domain thermoreflectance, TDTR [11–14], and the original frequency-domain thermoreflectance, FDTR [15,16]), and various improved laser pump-probe methods. Among the improved pump-probe methods, representative works involve the asymmetric-beam time--domain thermoreflectance (AB-TDTR [3,17], or the elliptical-beam TDTR [18,19]), the beam-offset time-domain thermoreflectance (BO-TDTR) [20,21], the beam-offset frequency-domain thermoreflectance (BO-FDTR) [2,22–25], and the spatial-domain thermoreflectance (SDTR) [26], etc. The most remarkable advantage of optical methods is the flexibility to adjust sample's orientation angles (or the relative positions of pump and probe laser spots), and the elliptical eccentricity of laser spots, thereby directly achieving a 360° scan of the in-plane anisotropic thermal conductivities [2,19].

Nevertheless, there are two inevitable limitations of these optical methods. First, probe signals of these optical methods (except the SDTR method) are generally sensitive to the thermophysical properties of

* Corresponding author.
E-mail address: caoby@mail.tsinghua.edu.cn (B.-Y. Cao).

https://doi.org/10.1016/j.ijheatmasstransfer.2023.124878
Received 30 June 2023; Received in revised form 18 October 2023; Accepted 24 October 2023

superficial structures, i.e., thermal conductivity and heat capacity of the metal transducer, and the transducer-sample thermal boundary resistance (TBR), owing to the laser's high repeating frequencies. This introduces additional errors in the thermal conductivity measurements. Meanwhile, these methods depend on multivariate fitting algorithms to derive the undetermined thermophysical properties, which are difficult to guarantee that the fitting results converge to the global optimum, introducing incalculable errors in the final measurement results. Regarding the novel SDTR method adopting low frequency, it is problematic to measure the cross-plane thermal conductivity due to insufficient sensitivity [26], despite SDTR overcoming the first of the two limitations of other optical methods.

In terms of electrical methods, the main ones applied to measure anisotropic thermal conductivity are the various harmonic methods developed from the classical 3ω method [27,28], including the multi-sensor 3ω method [29–36], the suspended 3ω method [28,29,37], and the two-sensor 2ω method [38–40]. Microfabricated devices [41,42] are also commonly used for anisotropic thermal conductivity measurements of low-dimensional materials. However, all the above electrical methods (except the two-sensor 2ω method) are affected by the error propagation from the thermal resistance of superficial structures (insulation layer, sensor-sample interface, etc.) to the final measurement results [38,39]. And similar to the optical methods, these electrical methods (except the microfabricated devices) also depend on multivariate fitting algorithms, which seriously challenges the accuracy of measured results. Moreover, it is difficult for the suspended 3ω method and the microfabricated devices to measure cross-plane thermal conductivity, unless one resorts to the classical 3ω method or the differential 3ω method [37,41].

Table 1 summarizes the comparison of currently available experimental methods. It is evident that a high-precision experimental method with universal applicability for measuring the isotropic or anisotropic thermal conductivities of solid materials is still lacking. Fortunately, it has been found in our prior work [43] and other related works [38,39] that the second harmonic (2ω) voltage signals across a DC detector is insensitive to the thermophysical properties of superficial structures, with the detector located near an AC heater. In this work, we propose the three-sensor 2ω method, which replaces multivariate fitting algorithms by the proposed Intersection Method, and inherits the spirit of 2ω signals to eliminate the error propagation from the thermal resistance of samples' superficial structures. Thus, the proposed three-sensor 2ω method effectively overcomes the limitations of existing methods as listed in Table 1.

This paper is organized as follows. First, the experimental system and measurement procedure (viz, the Intersection Method) are illustrated. Then the required guidelines for the three-sensor layout design are highlighted based on the signal sensitivity analysis. Finally, measurements are conducted on four monocrystalline semiconductor samples (i.e., Si, GaN, AlN, and β-Ga_2O_3) to verify the accuracy and applicability of the proposed three-sensor 2ω method.

2. Method

2.1. Experimental setup

Fig. 1 demonstrates the experimental system and sample structure of the proposed three-sensor 2ω method. The method is applied to measure the thermal conductivity of solid materials, regardless of their isotropic or anisotropic nature. As shown in Fig. 1(a), in order to prevent leakage and signal crosstalk between sensors, an insulation layer is deposited on the sample surface, except for well-insulating samples. Multiple three-sensor groups are then prepared on the surface along different characteristic directions of interest using lithography, sputtering, and lift-off processes. Each three-sensor group consists of three parallel metal sensors with different widths and distances (Fig. 1(b)) optimally designed based on sensitivity analysis. The outer two sensors function as heaters, with the wider one referred to as heater 1 and the narrower one as heater 2. A detector is situated between the two heaters, consistent with our prior works [43,44]. The substrate, insulation layer, and multiple three-sensor groups on the surface comprise the effective test sample, which allows for deriving thermal conductivities along different orientations of interest.

In this method, we merely adopt the second harmonic (2ω) voltage oscillations across the detector ($V_D^{2\omega}$) as the characteristic signal due to its good characteristics, hence the name "2ω method". Note that the commonly used third harmonic (3ω) voltage oscillations across the heaters are discarded in this method, which is explained in Sections 2.2 and 2.3. An AC current through the heater at frequency ω heats the sample at 2ω and produces the temperature oscillation at frequency 2ω, which makes resistances of the heater and detector contain 2ω AC components. This resistance oscillation times the DC current results in a small 2ω voltage oscillation $V_D^{2\omega}$ across the detector.

Fig. 1(b) shows the five characteristic geometric parameters of each three-sensor group that need to be engineered based on sensitivity analysis: the heater 1 width w_{H1}, the heater 1-detector distance d_{H1D}, the detector width w_D, the heater 2 width w_{H2}, and the heater 2-detector distance d_{H2D}. Sensitivity of the detector signal to the cross- and in-plane thermal conductivities (κ_{cr}, κ_{in}) can be adjusted directly by varying the heater width, the heater-detector distance, and the heating frequency f_H, which makes it feasible for the Intersection Method proposed in the next section. Specific guidelines for the layout design of each three-sensor group are detailed in Section 2.3 based on the sensitivity analysis in Supplementary Material (Section S1).

It is essential to select the length direction of each three-sensor group rationally. Owing to the large aspect ratio of each sensor (generally >15), the measured detector signal is insensitive to thermal conductivity parallel to the detector's length direction [28]. Hence, each three-sensor group is merely capable of deriving the cross-plane thermal conductivity, and the in-plane thermal conductivity perpendicular to the detector's length direction. In order to accurately derive the in-plane thermal conductivities along all orientations of interest, a corresponding

Table 1
Comparison of currently available techniques for measuring anisotropic thermal conductivity.

Category	Method	Sensitive to both cross- and in-plane thermal conductivities?	No multivariate fitting?	Invulnerable to the errors introduced by superficial structures?	Refs.
Optical	Original TDTR/FDTR	Yes	No	No	[11–16]
	AB-TDTR	Yes	No	No	[3,17-19]
	BO-TDTR/BO-FDTR	Yes	No	No	[2,20-25]
	SDTR	No	No	Yes	[26]
Electrical	Multi-sensor 3ω	Yes	No	No	[29–36]
	Suspended 3ω	No	No	No	[28,29, 37]
	Two-sensor 2ω	Yes	No	Yes	[38–40]
	Microfabricated devices	No	Yes	No	[41,42]
	Three-sensor 2ω	**Yes**	**Yes**	**Yes**	**This work**

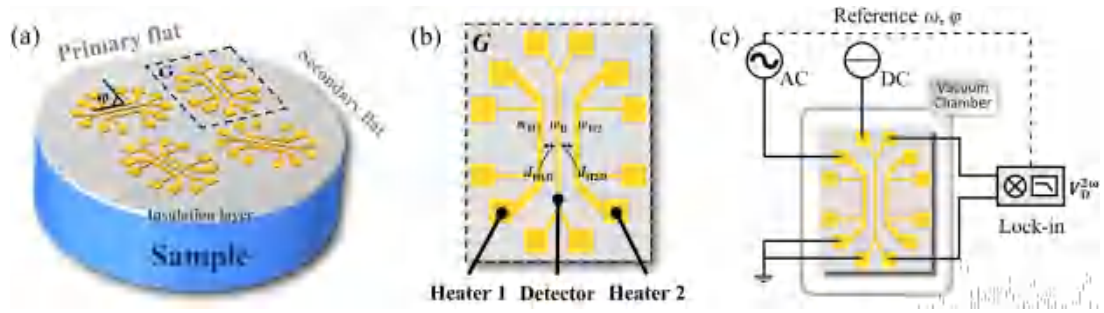

Fig. 1. Typical structure of a test sample and the experimental system of the three-sensor 2ω method. (a) Structure of a test sample and layout of the three-sensor groups. $\angle\varphi$ indicates the angle between the length direction of a three-sensor group and a given direction (e.g., the wafer secondary flat in this figure). For example, the dashed region G indicates the three-sensor group whose length direction is perpendicular to the primary flat (i.e., $\angle\varphi = 0$). Several three-sensor groups can be arbitrarily prepared upon the insulation layer, with their length directions along the orientations of interest. As shown in (a), three other groups are configured as parallel to the primary flat ($\angle\varphi = 90°$), $\angle\varphi = 30°$, and $\angle\varphi = 45°$, respectively. (b) Detail view of the three-sensor group G, where the five characteristic geometric parameters are illustrated. These geometric parameters need to be optimized based on sensitivity analysis. (c) Experimental system and circuit. The heaters (heater 1, heater 2) are energized individually by AC currents instead of synchronously during the test (i.e., heater 1 on & heater 2 off, or heater 1 off & heater 2 on), while the detector is energized by a constant DC throughout the measurement. This subfigure illustrates the circuit connection when the heater 1 (or heater 2) and the detector are working synchronously.

number of directions of the three-sensor group should be arranged. As shown in Fig. 1(a), an illustrative arrangement of four directions of the three-sensor group ($\angle\varphi$ = 0, 30°, 45°, 90°) is designed to derive the in-plane thermal conductivities along the four corresponding directions. $\angle\varphi$ indicates the angle between the length direction of a three-sensor group and a given direction (e.g., the wafer secondary flat used in this figure). Note that if ones are interested in the overall in-plane thermal conductivity of a lateral isotropic material instead of the thermal conductivity along a specific orientation, the directions of the three-sensor group can be arbitrarily chosen.

Based on the three-sensor layout on a sample shown in Fig. 1(a,b), the experimental system is built as Fig. 1(c). First, the sample is assembled in a vacuum chamber to avoid the errors introduced by convection and radiation, and to ensure accurate temperature control. Each three-sensor group is connected to the external circuit by a wire-bonding process, and the switching sequence of the two heaters is asynchronous. Specifically, the heater 1 is first energized individually by an AC current source (e.g., Keithley 6221) with the heater 2 power-off, while the detector is powered by a DC current source (e.g., Keithley 2450). And then, the heater 2 is energized individually by an AC current with the heater 1 power-off, while the detector continues to be powered by the DC current. The detector's 2ω signals are collected by a lock-in amplifier (e.g., SRS SR830), with the reference frequency and phase provided by the AC current source.

In addition, since the sample is covered with an insulation layer (e.g., amorphous SiO_2) or the sample itself is well-insulating, the 1ω voltage signals across the detector due to leakage from the heaters are negligible and are compatible with the lock-in amplifier's dynamic reserve. Hence, it is unnecessary to connect a variable resistor in series before the detector to subtract the 1ω common-mode voltage signal, as done in other existing 3ω-like methods [43,45].

2.2. Measurement procedure

The so-called "Intersection Method" is proposed here for measuring the cross- and in-plane thermal conductivities. The cross-plane thermal conductivity (κ_{cr}) and the in-plane thermal conductivity (κ_{in}) are derived by the intersection of the two $\kappa_{in}(\kappa_{cr})$ curves in $(\kappa_{cr}, \kappa_{in})$ coordinate, instead of being fitted by the multivariate fitting algorithms, which avoids the local optimum trap of multivariate fitting in principle. The two $\kappa_{in}(\kappa_{cr})$ curves are corresponding to the working sensor combinations (heater 1 & detector, or heater 2 & detector, respectively). The existence of the curve intersection is certain, provided the three-sensor layout is designed based on sensitivity analysis (as discussed in Section 2.3).

After the 2ω voltage signals across the DC detector ($V_D^{2\omega}$) are recorded by the lock-in amplifier, it is required to convert $V_D^{2\omega}$ into the 2ω temperature responses of the DC detector ($\theta_D^{2\omega}$, the temperature oscillation amplitudes), which is derived in literatures [38,40] and our prior works [43,46],

$$\theta_D^{2\omega} = \frac{\sqrt{2}V_D^{2\omega,\mathrm{rms}}}{I_D R_{D0}^{el}\beta_D}. \tag{1}$$

The superscript "rms" denotes the root mean square, I_D denotes the DC current across the detector, R_{D0}^{el} denotes the detector's resistance at the reference temperature, and β_D denotes the temperature coefficient of the detector's resistance (TCR).

Notice that the 3ω voltage signals across the AC heater ($V_H^{3\omega}$, corresponding to temperature responses of the AC heater $\theta_H^{2\omega} = \frac{2V_H^{3\omega,\mathrm{rms}}}{I_H^{\mathrm{rms}} R_{H0}^{el}\beta_H}$) is discarded in this method, though it is commonly used in other 3ω-like methods [27,28,30]. Since the accurate a priori thermal properties of the insulation layer are not available, the high sensitivity of the AC heater's 3ω voltage signals to thermal properties of the superficial structures (insulation layer, insulation layer-sample interface, etc.) will introduce a large error into the final measured results. In contrast, the 2ω voltage signal across the DC detector at a certain distance from the heater is a promising solution, since several studies have unraveled that the sensitivity of the detector's 2ω voltage signal to thermal properties of the superficial structures can be significantly suppressed [38,39,43]. Therefore, the 2ω signal across the DC detector is merely adopted in this study. The sensitivity analysis corresponding to this issue is illustrated in Supplementary Material (Section S1).

Based on the sample structure and experimental system shown in Fig. 1, the heating power of the heater 1 (Q_{H1}), the heating power of the heater 2 (Q_{H2}), and the corresponding temperature responses of the detector ($\theta_{D1}^{2\omega}$, $\theta_{D2}^{2\omega}$) are measured, respectively. After that, thermal conductivities of the sample along each direction of interest can be derived by the following steps, i.e., the Intersection Method. Fig. 2 illustrates steps (2) - (6) of the procedure.

(1) Construct a system in the finite element method (FEM) simulation that is consistent with the structure and boundary conditions of the sample.
(2) Set the heater 1's heating power (Q_{H1}) and the corresponding measured detector's temperature response ($\theta_{D1}^{2\omega}$) as the FEM simulation input.

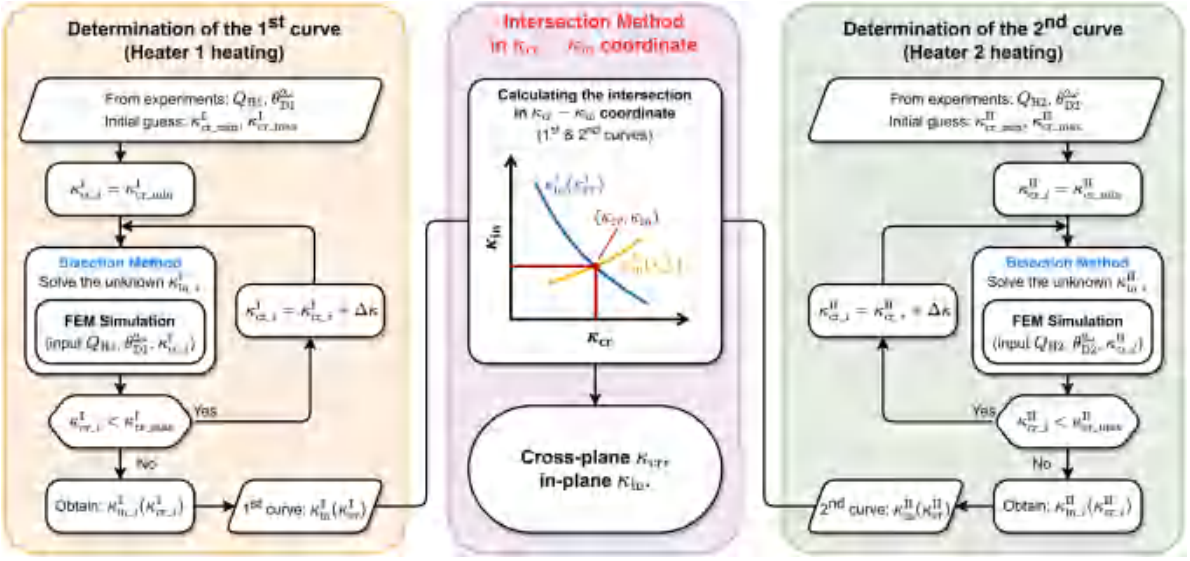

Fig. 2. The data processing procedure of the three-sensor 2ω method. The core is the so-called "Intersection Method", which determines the cross- and in-plane thermal conductivities from the intersection of the two $\kappa_{in}(\kappa_{cr})$ curves. The existence of the curve intersection is certain, provided the three-sensor layout is designed based on sensitivity analysis. Note that the routine shown in this figure needs to perform on each three-sensor group respectively to derive the anisotropic in-plane thermal conductivity along each direction of interest. The κ_{in} and κ_{cr} are mathematically equivalent, so one can arbitrarily adopt the $\kappa_{in}(\kappa_{cr})$ or $\kappa_{cr}(\kappa_{in})$ curve according to specific conditions.

(3) In FEM, continuously adjust the input of cross-plane thermal conductivity (κ_{cr}^{I}), and then solve the nonlinear monadic equation $f(\kappa_{in}^{I}|\kappa_{cr}=\kappa_{cr}^{I}, Q_H=Q_{H1})=\theta_{D1}^{2\omega}$ numerically (e.g., by Bisection Algorithm), to derive the unknown in-plane thermal conductivity (κ_{in}^{I}). Thus, the first curve $\kappa_{in}^{I}(\kappa_{cr}^{I})$ is obtained.

(4) Set the heater 2's heating power (Q_{H2}) and the corresponding measured detector's temperature response ($\theta_{D2}^{2\omega}$) as the FEM simulation input.

(5) In FEM, continuously adjust the input of cross-plane thermal conductivity (κ_{cr}^{II}), and then solve the nonlinear monadic equation $f(\kappa_{in}^{II}|\kappa_{cr}=\kappa_{cr}^{II}, Q_H=Q_{H2})=\theta_{D2}^{2\omega}$ numerically, to derive the unknown in-plane thermal conductivity (κ_{in}^{II}). Thus, the second curve $\kappa_{in}^{II}(\kappa_{cr}^{II})$ is obtained.

(6) Plot the two curves obtained in steps (3) and (5) in the $(\kappa_{cr},\ \kappa_{in})$ coordinate, and their intersection indicates the measured cross- and in-plane thermal conductivities of the sample. Note that the in-plane thermal conductivity is normal to the length direction of the corresponding three-sensor group.

(7) For the three-sensor groups along different directions, repeat steps (2) to (6) to obtain the cross- and in-plane thermal conductivities corresponding to the length direction of each three-sensor group.

The FEM model is illustrated in in Supplementary Material (Section S4.4). In brief, the cross- and in-plane thermal conductivities are derived from the intersection of the two $\kappa_{in}(\kappa_{cr})$ curves in $(\kappa_{cr}, \kappa_{in})$ coordinate. Note that the κ_{in} and κ_{cr} are mathematically equivalent, so one can arbitrarily adopt the $\kappa_{in}(\kappa_{cr})$ or $\kappa_{cr}(\kappa_{in})$ curve according to specific conditions. It is also feasible to apply the analytical solutions of harmonic heating [30,47] rather than FEM simulations for better calculation efficiency, which does not affect the procedure of the Intersection Method.

Furthermore, if one wishes the intersection of two functions to be legible enough, the difference between the first-order derivatives of the two curves ($\frac{\partial\kappa_{cr}}{\partial\kappa_{in}}$, or equivalently the relative sensitivities $\frac{\partial\ln(\kappa_{cr})}{\partial\ln(\kappa_{in})}$) near the intersection point needs to be maximized. This lays a foundation for optimizing the three-sensor layout design in this method, which is detailed in the next section.

2.3. Three-sensor layout design

Guidelines for optimizing the three-sensor layout design and selecting the heating frequency are discussed in this section. In Section 2.2, we have stated that the solution to improving the accuracy of calculating intersection coordinates is to maximize the discrepancy of the first-order derivatives ($\frac{\partial\kappa_{cr}}{\partial\kappa_{in}}$, or the relative sensitivities $\frac{\partial\ln(\kappa_{cr})}{\partial\ln(\kappa_{in})}$) between the two curves $\kappa_{in}^{I}(\kappa_{cr}^{I})$ and $\kappa_{in}^{II}(\kappa_{cr}^{II})$ at the intersection, and the prerequisite for this strategy is optimizing the three-sensor layout design and selecting the heating frequencies.

The three-sensor layout design is determined by three characteristic geometric parameters: the heater width w_H, the heater-detector distance d_{HD}, and the detector width w_D, while the heating frequency f_H is also an adjustable parameter. Hence, based on the detailed sensitivity analysis of sensors' signals and the resulting four feasible regions (Regions A, B, D, E shown in Fig. S1 in Supplementary Material), guidelines for the three-sensor layout design and the selection of heating frequency are summarized as follows, and the corresponding mind map is illustrated in Fig. 3.

(1) To minimize $\frac{\partial\ln(\kappa_{cr})}{\partial\ln(\kappa_{in})}$: A wide heater 1 is arranged upon the sample surface, and a narrow detector 1 is located at a long distance from heater 1. Under this condition, the relative sensitivity ($\frac{\partial\ln(\kappa_{cr}^{I})}{\partial\ln(\kappa_{in}^{I})}$) of detector 1's 2ω signal approaches 0, with heater 1 individually heating the sample at a relatively high frequency.

(2) To maximize $\frac{\partial\ln(\kappa_{cr})}{\partial\ln(\kappa_{in})}$: A narrow heater 2 is arranged, and a narrow detector 2 is located at a medium distance from heater 2. Under this condition, the relative sensitivity ($\frac{\partial\ln(\kappa_{cr}^{II})}{\partial\ln(\kappa_{in}^{II})}$) of detector 2's 2ω signal approaches a large value, with heater 2 individually heating the sample at a low frequency.

(3) To restrain sensitivity to the effective thermal conductivity of insulation layer (κ_{ins}): The distance between heater 1(heater 2) and detector 1(detector 2) should not be too small.

(4) To simplify layout design: detector 1 and detector 2 can be merged into a single detector to simplify the sensor layout without affecting the measurement procedure and precision.

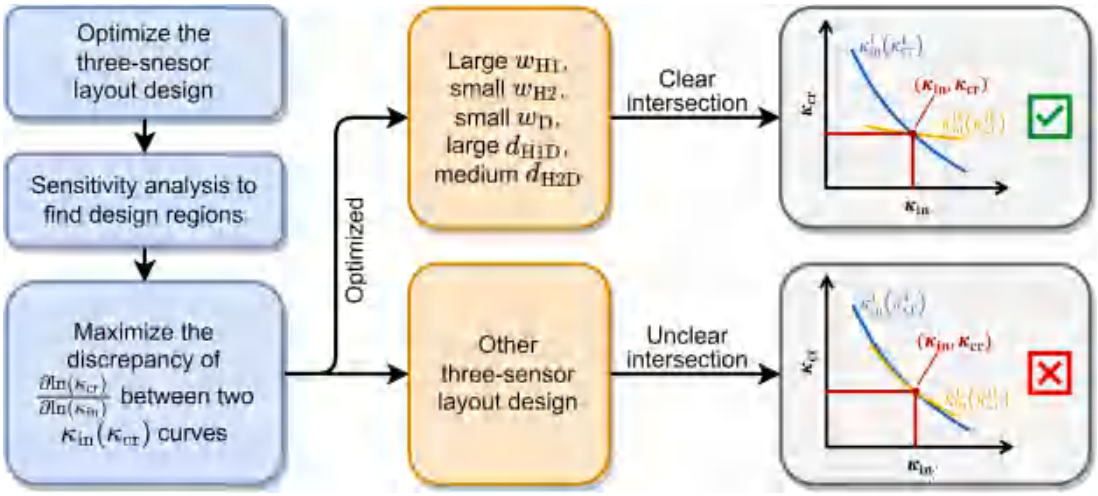

Fig. 3. Mind map of optimizing the three-sensor layout of the three-sensor 2ω method. The key criterion is to maximize the discrepancy of $\frac{\partial \ln(\kappa_{cr})}{\partial \ln(\kappa_{in})}$ between the two curves (viz, $\kappa_{in}^{I}(\kappa_{cr}^{I})$, $\kappa_{in}^{II}(\kappa_{cr}^{II})$) at the intersection, thereby making the intersection of two curves clear and legible. Here, w_{H1}, w_{H2}, w_D, d_{H1D}, d_{H2D} are consistent with Fig. 1(b), and the "optimized" parameter combination is a representative example within the feasible design space.

Note that the geometric parameter combination of three-sensor layout discussed here (i.e., large w_{H1}, small w_{H2}, small w_D, large d_{H1D}, medium d_{H2D}) is a representative example within the feasible design space, which is a handy design compatible with the stepper lithography and lift-off processes. Moreover, κ_{ins} includes contributions from the sensor-insulation layer TBR, the thermal resistance of insulation layer, and the insulation layer-sample TBR [43].

Finally, the three-sensor layout consisting of a wide heater 1, a narrow heater 2, and a narrow detector, incorporating the appropriate distances and heating frequencies are engineered. As discussed before, the three-sensor design can eliminate the error propagation from uncertainties in the thermal resistance of superficial structures, and this is demonstrated in Supplementary Material (Section S2, S5).

3. Results and discussions

To verify the accuracy and reliability of the proposed three-sensor 2ω method, four typical monocrystalline semiconductor substrates, i.e., (100) Si wafer, (0001) GaN wafer, (0001) AlN wafer, and (010) β-Ga_2O_3 substrate, are measured at 300 K. The four samples are prepared by different processes, among which the Si and β-Ga_2O_3 are fabricated by the Edge-defined Film-fed Growth (EFG) process [48], the GaN by the Hydride Vapor Phase Epitaxy (HVPE) process [49], and the AlN by the Physical Vapor Transport (PVT) process [50]. These wafers are purchased from corresponding companies.

To eliminate the leakage current and signal crosstalk between sensors, an amorphous SiO_2 insulation layer of ~40 nm is first deposited upon each sample by the Plasma Enhanced Chemical Vapor Deposition (PECVD) process [43]. Then the multiple three-sensor groups are fabricated upon the SiO_2 surface via lithography, magnetron sputtering, and lift-off processes successively [43,46], as illustrated in Supplementary Material (Section S3.1), with the layouts and heating frequencies being optimized following the design guidelines depicted in Section 2.3. The material of each sensor is 90 nm Au/10 nm Cr (Cr for adhesion), and the actual patterns of three-sensor groups are shown in Fig. 4. For convenience, the material and deposition method of the insulation layers and of the metal sensors are all the same in four samples. Thus, the complete test samples are prepared.

The specific dimensions of three-sensor groups are characterized with the scanning electron microscope (SEM) and are detailed in Supplementary Material (Section S3.2). However, if one wants to measure a novel material with irregular shapes and unavailable wafers, it is necessary to conduct an X-ray diffraction (XRD) characterization to determine the feature crystal orientations of samples [51] before designing the sensor directions accordingly.

After the sample preparation and experimental circuit connection, the TCR (β) of all sensors need to be calibrated (Section S4.1 in Supplementary Material). After that, an AC current is first applied to the heater 1 (with frequency $f_{H1} = 2000$ Hz) in one of the three-sensor groups on a sample with the heater 2 power-off, and a constant DC

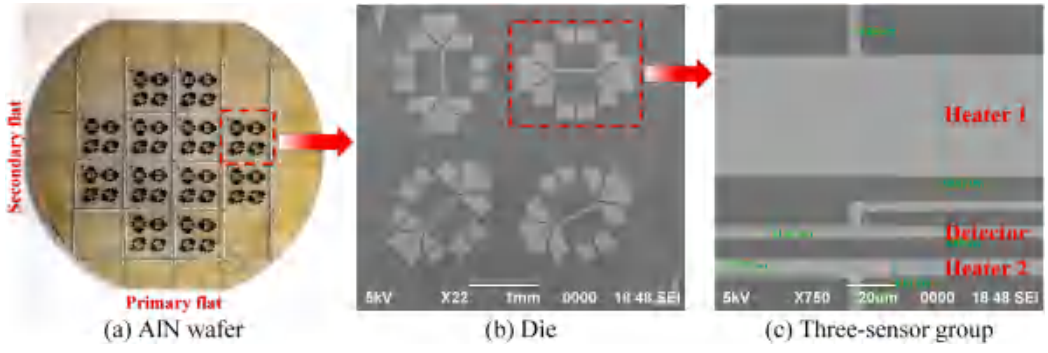

Fig. 4. The practical three-sensor groups on the AlN wafer. (a) The entire wafer with a primary flat (along a-axis, i.e., the $[1\bar{1}00]$ orientation) and a secondary flat (along m-axis). Twelve square dies with four three-sensor groups along different directions within them ($\angle\varphi = 0,\ 30^{\circ},\ 45^{\circ},\ 90^{\circ}$) are fabricated upon the surface. (b) One of the dies on the wafer, and the triangle in the top left corner implies the direction normal to primary flat ($\angle\varphi = 0$). (c) Detail view of the three-sensor group parallel to the primary flat within a die.

current is applied to the detector. Next, an AC current is applied to the heater 2 (f_{H2} = 300 Hz) in the same three-sensor group with the heater 1 power-off, and the detector is continuously powered by the DC. The frequency of AC currents chosen for measuring all four samples are the same, whose universality is validated by the sensitivity analysis discussed in Supplementary Material (Section S1). The 2ω signals across the detector are recorded by a lock-in amplifier and converted into the temperature response signals ($\theta_{D1}^{2\omega}$, $\theta_{D2}^{2\omega}$) according to Eq. (1).

Then following the measurement procedure given in Section 2.2, a FEM simulation model is built as shown in Supplementary Material (Section S4.4), and the corresponding two curves $\kappa_{in}^{I}(\kappa_{cr}^{I})$, $\kappa_{in}^{II}(\kappa_{cr}^{II})$ can be calculated numerically (e.g., by the "fzero()" function in MATLAB®). Note that the κ_{in} and κ_{cr} are mathematically equivalent, so one can arbitrarily adopt the $\kappa_{in}(\kappa_{cr})$ or $\kappa_{cr}(\kappa_{in})$ curve for convenience.

In the FEM simulation, the thermal conductivity of each metal sensor is calculated from its electrical conductivity by the Wiedemann-Franz Law as discussed in Supplementary Material (Section S4.2). The heat capacity and density of each material are referred to the SpringerMaterials database and the literature [19,52], and the effective thermal conductivity of SiO_2 layer (κ_{ins}) is set to be 1.2 W/m K referring to our prior work [43], due to the same fab, growth process and SiO_2 structure. As explained before, κ_{ins} includes the sensor-SiO_2 TBR, the thermal resistance of SiO_2, and the SiO_2-substrate TBR.

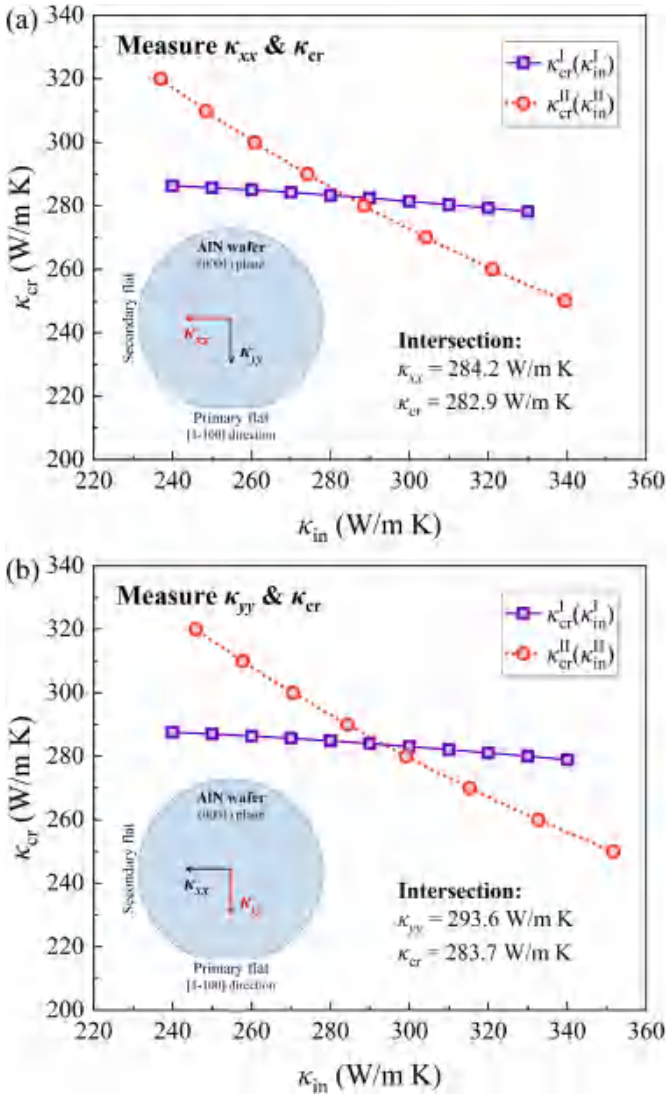

Fig. 5. Determine the cross- and in-plane thermal conductivities of the AlN wafer via the Intersection Method. (a) Determine the cross-plane thermal conductivity κ_{cr} and the in-plane thermal conductivity parallel to the primary flat κ_{xx}. (b) Determine κ_{cr} and κ_{yy}. Average of the two κ_{cr} measurements is chosen as the final κ_{cr} result.

According to the Intersection Method, the cross-plane thermal conductivity and the in-plane thermal conductivity normal to the length direction of a three-sensor group are derived from the intersection coordinate of two $\kappa_{cr}(\kappa_{in})$ curves (as shown in Fig. 5). By repeating the Intersection Method for all the three-sensor groups along different directions, comprehensive information about the cross- and in-plane thermal conductivities of the test sample can be obtained finally.

The measured thermal conductivities at room temperature are listed in Tables 2 and 3, and the error analysis is summarized in Supplementary Material (Section S5). For sample Si, GaN, and AlN, the thermal conductivities are all in good agreement with literatures [26,53–66]. Specifically, the κ_{xx}, κ_{yy}, κ_{zz} are along the orientations that parallel to the wafer primary flat (Si: [110], GaN or AlN: [1$\bar{1}$00]), parallel to the wafer secondary flat (Si: [1$\bar{1}$0], GaN or AlN: [11$\bar{2}$0]), and normal to the wafer plane (Si: [001], GaN or AlN: [0001]), respectively. In addition, the thermal conductivities of these three samples are all approximately isotropic.

Unlike the above three materials, the thermal conductivity of β-Ga_2O_3 is three-dimensional anisotropic, which stems from its monoclinic lattice [13,67]. For the several characteristic crystal orientations (e.g., [010], [100]), the corresponding measurements are listed in Table 3. Based on the measured thermal conductivities along each main orientation, the components of thermal conductivity tensor (κ_{xx}, κ_{xy}, κ_{yy}, and κ_{zz}) are derived according to the geometric relationships ($\kappa_{in}(\theta) = \kappa_{xx}\cos^2\theta + 2\kappa_{xy}\sin\theta\cos\theta + \kappa_{yy}\sin^2\theta$, $\kappa_{zz} = \kappa_{cr}$) [2,19,67]. Correspondingly, the entire thermal conductivity tensor of β-Ga_2O_3 can be determined as shown in Table 3. These results are consistent with literatures as well [13,19]. Our results are slightly higher than Jiang's [19], which may attribute to the differences in doping conditions (ours: undoped, Jiang's: Si-doped).

Fig. 6 illustrates the comparison between the measured thermal conductivities in this study with other measurements and numerical simulations. In Fig. 6(a), measured thermal conductivities of the four materials are laterally compared with literatures, and error bars are almost covered by data points. Moreover, $\kappa_{in}(\theta)$ of the β-Ga_2O_3 (010) plane are solely compared with literatures as shown in Fig. 6(b), where our measured $\kappa_{in}(\theta)$ falls between those of Jiang et al. [19] and Guo et al. [13]. Meanwhile, our results are slightly lower than those of ShengBTE calculations based on the Gaussian approximation potential (GAP) performed by Liu et al. [67], since the simulation neglects lattice defects (e.g., isotope, unintentionally dope) distributing within the crystal. In summary, results obtained by the three-sensor 2ω method are consistent with the representative data available in the literatures, which validates the accuracy and reliability of this method.

Table 2
Measured thermal conductivities of the three approximately isotropic materials (300 K). (κ_{cr}: cross-plane thermal conductivity, κ_{xx}: thermal conductivity parallel to the primary flat, κ_{yy}: thermal conductivity parallel to the secondary flat, κ_{ave}: effective bulk thermal conductivity)

Sample	Thermal conductivity (W/m K)				
	κ_{cr}	κ_{xx}	κ_{yy}	κ_{ave}	κ_{ref}
Si	156.8 ± 4.4	146.5 ± 6.0	141.0 ± 5.8	148.1 ± 5.4	145 ± 7 [26]
GaN	201.4 ± 5.6	203.7 ± 8.3	208.5 ± 8.5	204.5 ± 7.5	211 ± 5 [59]
AlN	283.3 ± 7.2	284.2 ± 10.5	293.6 ± 10.8	287.0 ± 9.5	297 ± 7 [62]

Table 3
Measured thermal conductivities of the sample β-Ga_2O_3 (300 K).

Orientation	Thermal conductivity (W/m K)		
	κ	κ tensor	κ_{ref}
x-axis ([100])	10.5 ± 0.5	$\begin{bmatrix} 10.5 & -0.8 & 0 \\ -0.8 & 14.4 & 0 \\ 0 & 0 & 24.8 \end{bmatrix}$	9.5 ± 1.8 [19]
y-axis	14.4 ± 0.8		≈ 13.3 ± 1.8 [19]
z-axis ([010])	24.8 ± 0.8		22.5 ± 2.5 [19]
45° to *x*, *y* (near [102])	11.7 ± 0.6		≈ 11.0 ± 1.8 [19]

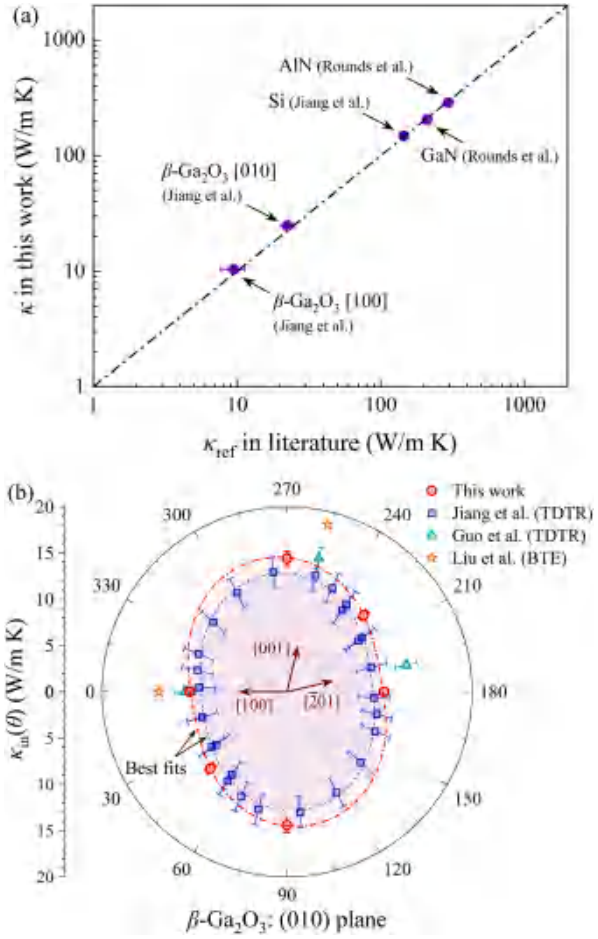

Fig. 6. Comparison between the measured thermal conductivities with the literature. (a) A lateral comparison of the four materials' thermal conductivities with the literature. (b) A detailed comparison of in-plane thermal conductivity (κ_{in}) within the β-Ga_2O_3 (010) plane with the literature. The red dot dash ellipse shows the best fit of $\kappa_{in}(\theta)$ measured in this work, and is slightly higher than that of Jiang et al. [19] (blue dash ellipse) ascribing to different doping conditions. The orange marks show the ShengBTE calculations of monocrystalline β-Ga_2O_3 based on the Gaussian approximation potential (GAP) [67].

4. Conclusions

In this work, we present the three-sensor 2ω method for measuring the thermal conductivity of solid materials, regardless of isotropy or anisotropy. To implement this method, multiple three-sensor groups are fabricated on the sample surface along different directions of interest. Each group contains three parallel metal sensors with optimized widths and distances according to design guidelines. The outer two sensors serve as AC heaters, while the middle sensor acts as a DC detector. The 2ω voltage signals across the detector are measured, and then data are processed using the proposed Intersection Method to obtain cross- and in-plane thermal conductivities along the directions of interest. Based on this method, four typical monocrystalline semiconductors, namely Si, GaN, AlN, and β-Ga_2O_3, are measured, and the results are consistent with literatures, verifying the accuracy and reliability of this method. The application of the detector's 2ω instead of the heater's 3ω signals eliminates the errors propagated from the uncertainties of thermal resistance in superficial structures (insulation layer, insulation layer-sample interface, etc.). In addition, this method replaces the commonly used multivariate fitting algorithms with the proposed Intersection Method, avoiding the local optimum trap of multivariate fitting. Therefore, the three-sensor 2ω method overcomes the main limitations of existing methods. This method will provide a comprehensive and universal solution for the thermal conductivity measurement of solid materials.

CRediT authorship contribution statement

Guang Yang: Conceptualization, Methodology, Software, Validation, Formal analysis, Investigation, Resources, Data curation, Writing – original draft, Writing – review & editing, Visualization. **Bing-Yang Cao:** Resources, Writing – review & editing, Supervision, Project administration, Funding acquisition.

Declaration of Competing Interest

The authors declare that they have no known competing financial interests or personal relationships that could have appeared to influence the work reported in this paper.

Data availability

Data will be made available on request.

Acknowledgments

This work was financially supported by the National Natural Science Foundation of China (Grant No. 51825601, U20A20301).

Supplementary materials

Supplementary material associated with this article can be found, in the online version, at doi:10.1016/j.ijheatmasstransfer.2023.124878. See the supplementary material for the sensitivity analysis and the feasible regions for the three-sensor layout design (Section S1), the robustness analysis on the influence of insulation layer's thermal resistance (Section S2), the fabrication of the three-sensor layout (Section S3), the measurement details (Section S4), and the error analysis (Section S5).

References

[1] D.G. Cahill, P.V. Braun, G. Chen, D.R. Clarke, S. Fan, K.E. Goodson, P. Keblinski, W. P. King, G.D. Mahan, A. Majumdar, H.J. Maris, S.R. Phillpot, E. Pop, L. Shi, Nanoscale thermal transport. II. 2003–2012, Appl. Phys. Rev. 1 (1) (2014), 011305.
[2] L. Tang, C. Dames, Anisotropic thermal conductivity tensor measurements using beam-offset frequency domain thermoreflectance (BO-FDTR) for materials lacking in-plane symmetry, Int. J. Heat Mass Transf 164 (2021), 120600.
[3] M. Li, J.S. Kang, Y. Hu, Anisotropic thermal conductivity measurement using a new asymmetric-beam time-domain thermoreflectance (AB-TDTR) method, Rev. Sci. Instrum. 89 (8) (2018), 084901.
[4] Y. Won, J. Cho, D. Agonafer, M. Asheghi, K.E. Goodson, Fundamental cooling limits for high power density gallium nitride electronics, IEEE Trans. Comp. Packag. Manuf. Technol. 5 (6) (2015) 737–744.

[5] G. Wehmeyer, T. Yabuki, C. Monachon, J. Wu, C. Dames, Thermal diodes, regulators, and switches: physical mechanisms and potential applications, Appl. Phys. Rev. 4 (4) (2017), 041304.
[6] J.H. Chu, J.G. Analytis, K. De Greve, P.L. McMahon, Z. Islam, Y. Yamamoto, I. R. Fisher, In-plane resistivity anisotropy in an underdoped iron arsenide superconductor, Science 329 (5993) (2010) 824–826.
[7] D. Kraemer, B. Poudel, H.P. Feng, J.C. Caylor, B. Yu, X. Yan, Y. Ma, X. Wang, D. Wang, A. Muto, K. McEnaney, M. Chiesa, Z. Ren, G. Chen, High-performance flat-panel solar thermoelectric generators with high thermal concentration, Nat. Mater. 10 (7) (2011) 532–538.
[8] M. Wang, S. Lin, Anisotropic and ultralow phonon thermal transport in organic–inorganic hybrid perovskites: atomistic insights into solar cell thermal management and thermoelectric energy conversion efficiency, Adv. Funct. Mater. 26 (29) (2016) 5297–5306.
[9] L.D. Zhao, S.H. Lo, Y. Zhang, H. Sun, G. Tan, C. Uher, C. Wolverton, V.P. Dravid, M. G. Kanatzidis, Ultralow thermal conductivity and high thermoelectric figure of merit in SnSe crystals, Nature 508 (7496) (2014) 373–377.
[10] X. Yan, B. Poudel, Y. Ma, W.S. Liu, G. Joshi, H. Wang, Y. Lan, D. Wang, G. Chen, Z. F. Ren, Experimental Studies on Anisotropic Thermoelectric Properties and Structures of n-Type Bi2Te2.7Se0.3, Nano Lett. 10 (9) (2010) 3373–3378.
[11] A.J. Schmidt, X. Chen, G. Chen, Pulse accumulation, radial heat conduction, and anisotropic thermal conductivity in pump-probe transient thermoreflectance, Rev. Sci. Instrum. 79 (11) (2008), 114902.
[12] X. Qian, P. Jiang, R. Yang, Anisotropic thermal conductivity of 4H and 6H silicon carbide measured using time-domain thermoreflectance, Mater. Today Phys. 3 (2017) 70–75.
[13] Z. Guo, A. Verma, X. Wu, F. Sun, A. Hickman, T. Masui, A. Kuramata, M. Higashiwaki, D. Jena, T. Luo, Anisotropic thermal conductivity in single crystal β-gallium oxide, Appl. Phys. Lett. 106 (11) (2015), 111909.
[14] P. Jiang, X. Qian, R. Yang, Time-domain thermoreflectance (TDTR) measurements of anisotropic thermal conductivity using a variable spot size approach, Rev. Sci. Instrum. 88 (7) (2017), 074901.
[15] A.J. Schmidt, R. Cheaito, M. Chiesa, A frequency-domain thermoreflectance method for the characterization of thermal properties, Rev. Sci. Instrum. 80 (9) (2009), 094901.
[16] E. Ziade, Wide bandwidth frequency-domain thermoreflectance: Volumetric heat capacity, anisotropic thermal conductivity, and thickness measurements, Rev. Sci. Instrum. 91 (12) (2020), 124901.
[17] L.A. Pérez, K. Xu, M.R. Wagner, B. Dörling, A. Perevedentsev, A.R. Goñi, M. Campoy-Quiles, M.I. Alonso, J.S. Reparaz, Anisotropic thermoreflectance thermometry: A contactless frequency-domain thermoreflectance approach to study anisotropic thermal transport, Rev. Sci. Instrum. 93 (3) (2022), 034902.
[18] P. Jiang, X. Qian, R. Yang, A new elliptical-beam method based on time-domain thermoreflectance (TDTR) to measure the in-plane anisotropic thermal conductivity and its comparison with the beam-offset method, Rev. Sci. Instrum. 89 (9) (2018), 094902.
[19] P. Jiang, X. Qian, X. Li, R. Yang, Three-dimensional anisotropic thermal conductivity tensor of single crystalline β-Ga2O3, Appl. Phys. Lett. 113 (23) (2018), 232105.
[20] J.P. Feser, D.G. Cahill, Probing anisotropic heat transport using time-domain thermoreflectance with offset laser spots, Rev. Sci. Instrum. 83 (10) (2012), 104901.
[21] J.P. Feser, J. Liu, D.G. Cahill, Pump-probe measurements of the thermal conductivity tensor for materials lacking in-plane symmetry, Rev. Sci. Instrum. 85 (10) (2014), 104903.
[22] B. Li, L. Pottier, J.P. Roger, D. Fournier, K. Watari, K. Hirao, Measuring the anisotropic thermal diffusivity of silicon nitride grains by thermoreflectance microscopy, J. Eur. Ceram. Soc. 19 (8) (1999) 1631–1639.
[23] D. Rodin, S.K. Yee, Simultaneous measurement of in-plane and through-plane thermal conductivity using beam-offset frequency domain thermoreflectance, Rev. Sci. Instrum. 88 (1) (2017), 014902.
[24] M. Rahman, M. Shahzadeh, P. Braeuninger-Weimer, S. Hofmann, O. Hellwig, S. Pisana, Measuring the thermal properties of anisotropic materials using beam-offset frequency domain thermoreflectance, J. Appl. Phys. 123 (24) (2018), 245110.
[25] X. Qian, Z. Ding, J. Shin, A.J. Schmidt, G. Chen, Accurate measurement of in-plane thermal conductivity of layered materials without metal film transducer using frequency domain thermoreflectance, Rev. Sci. Instrum. 91 (6) (2020), 064903.
[26] P. Jiang, D. Wang, Z. Xiang, R. Yang, H. Ban, A new spatial-domain thermoreflectance method to measure a broad range of anisotropic in-plane thermal conductivity, Int. J. Heat Mass Transfer 191 (2022), 122849.
[27] D.G. Cahill, Thermal conductivity measurement from 30 to 750 K: the 3ω method, Rev. Sci. Instrum. 61 (2) (1990) 802–808.
[28] C. Dames, Measuring the thermal conductivity of thin films: 3 omega and related electrothermal methods, Annu. Rev. Heat Transfer 16 (2013) 7–49.
[29] K. Kurabayashi, M. Asheghi, M. Touzelbaev, K.E. Goodson, Measurement of the thermal conductivity anisotropy in polyimide films, J. Microelectromech. Syst. 8 (2) (1999) 180–191.
[30] T. Borca-Tasciuc, A.R. Kumar, G. Chen, Data reduction in 3ω method for thin-film thermal conductivity determination, Rev. Sci. Instrum. 72 (4) (2001) 2139–2147.
[31] M. Slomski, N. Blumenschein, P.P. Paskov, J.F. Muth, T. Paskova, Anisotropic thermal conductivity of β-Ga2O3 at elevated temperatures: effect of Sn and Fe dopants, J. Appl. Phys. 121 (23) (2017), 235104.
[32] G.P. Su, X.H. Zheng, L. Qiu, D.W. Tang, J. Zhu, Measurement of thermal conductivity of anisotropic SiC crystal, Int. J. Thermophys. 34 (12) (2013) 2334–2342.
[33] S. Yamaguchi, T. Shiga, S. Ishioka, T. Saito, T. Kodama, J. Shiomi, Anisotropic thermal conductivity measurement of organic thin film with bidirectional 3ω method, Rev. Sci. Instrum. 92 (3) (2021), 034902.
[34] C. Forsythe, M.P. Gordon, J.J. Urban, 3ω techniques for measurement of volumetric heat capacity and anisotropic thermal conductivity of a solution processable, hybrid organic/inorganic film, Te-PEDOT:PSS, J. Appl. Phys. 131 (10) (2022), 105109.
[35] B. Olson, S. Graham, Extending the 3 omega method to measure thermal conductivity anisotropy in three dimensions. ASME 2005 Summer Heat Transfer Conference collocated with the ASME 2005 Pacific Rim Technical Conference and Exhibition on Integration and Packaging of MEMS, NEMS, and Electronic Systems, American Society of Mechanical Engineers Digital Collection, 2009, pp. 29–35.
[36] V. Mishra, C.L. Hardin, J.E. Garay, C. Dames, A 3 omega method to measure an arbitrary anisotropic thermal conductivity tensor, Rev. Sci. Instrum. 86 (5) (2015), 054902.
[37] S. Kommandur, S. Yee, A suspended 3-omega technique to measure the anisotropic thermal conductivity of semiconducting polymers, Rev. Sci. Instrum. 89 (11) (2018), 114905.
[38] A.T. Ramu, J.E. Bowers, A "2-omega" technique for measuring anisotropy of thermal conductivity, Rev. Sci. Instrum. 83 (12) (2012), 124903.
[39] A.T. Ramu, J.E. Bowers, Analysis of the "3-Omega" method for substrates and thick films of anisotropic thermal conductivity, J. Appl. Phys. 112 (4) (2012), 043516.
[40] M. Handwerg, R. Mitdank, Z. Galazka, S.F. Fischer, Temperature-dependent thermal conductivity in Mg-doped and undoped β-Ga2O3 bulk-crystals, Semicond. Sci. Technol. 30 (2) (2015), 024006.
[41] S. Kwon, J. Zheng, M.C. Wingert, S. Cui, R. Chen, Unusually High and Anisotropic Thermal Conductivity in Amorphous Silicon Nanostructures, ACS Nano 11 (3) (2017) 2470–2476.
[42] S. Lee, F. Yang, J. Suh, S. Yang, Y. Lee, G. Li, H.Sung Choe, A. Suslu, Y. Chen, C. Ko, J. Park, K. Liu, J. Li, K. Hippalgaonkar, J.J. Urban, S. Tongay, J. Wu, Anisotropic in-plane thermal conductivity of black phosphorus nanoribbons at temperatures higher than 100 K, Nat. Commun. 6 (1) (2015) 8573.
[43] G. Yang, B.Y. Cao, Three-sensor 3ω-2ω method for the simultaneous measurement of thermal conductivity and thermal boundary resistance in film-on-substrate heterostructures, J. Appl. Phys. 133 (4) (2023), 045104.
[44] Y.B. Liu, H.L. Liang, L. Yang, G. Yang, H.A. Yang, S. Song, Z.X. Mei, G. Csányi, B. Y. Cao, Unraveling thermal transport correlated with atomistic structures in amorphous gallium oxide via machine learning combined with experiments, Adv. Mater. 35 (24) (2023), 2210873.
[45] C.E. Raudzis, F. Schatz, D. Wharam, Extending the 3ω method for thin-film analysis to high frequencies, J. Appl. Phys. 93 (10) (2003) 6050–6055.
[46] Y.C. Hua, B.Y. Cao, A two-sensor 3ω-2ω method for thermal boundary resistance measurement, J. Appl. Phys. 129 (12) (2021), 125107.
[47] J. Ordonez-Miranda, L. Jalabert, Y. Wu, S. Volz, M. Nomura, Analytical integration of the heater and sensor 3ω signals of anisotropic bulk materials and thin films, J. Appl. Phys. 133 (20) (2023).
[48] A. Kuramata, K. Koshi, S. Watanabe, Y. Yamaoka, T. Masui, S. Yamakoshi, High-quality β-Ga_2O_3 single crystals grown by edge-defined film-fed growth, Jpn. J. Appl. Phys. 55 (12) (2016) 1202A1202.
[49] A. Denis, G. Goglio, G. Demazeau, Gallium nitride bulk crystal growth processes: a review, Mater. Sci. Eng. R Rep. 50 (6) (2006) 167–194.
[50] D. Fu, D. Lei, Z. Li, G. Zhang, J. Huang, X. Sun, Q. Wang, D. Li, J. Wang, L. Wu, Toward Φ56 mm Al-polar AlN single crystals grown by the homoepitaxial PVT method, Cryst. Growth Des. 22 (5) (2022) 3462–3470.
[51] H. Berger, H.A. Bradaczek, H. Bradaczek, Omega-Scan: an X-ray tool for the characterization of crystal properties, J. Mater. Sci. Mater. Electron. 19 (1) (2008) 351–355.
[52] D. Sedmidubský, J. Leitner, P. Svoboda, Z. Sofer, J. Macháček, Heat capacity and phonon spectra of $A^{III}N$, J. Therm. Anal. Calorim. 95 (2) (2009) 403–407.
[53] H.R. Shanks, P.D. Maycock, P.H. Sidles, G.C. Danielson, Thermal Conductivity of Silicon from 300 to 1400°K, Phys. Rev. 130 (5) (1963) 1743–1748.
[54] A.V. Inyushkin, A.N. Taldenkov, A.M. Gibin, A.V. Gusev, H.J. Pohl, On the isotope effect in thermal conductivity of silicon, Phys. Stat. Solidi (C) 1 (11) (2004) 2995–2998.
[55] J.L. Braun, D.H. Olson, J.T. Gaskins, P.E. Hopkins, A steady-state thermoreflectance method to measure thermal conductivity, Rev. Sci. Instrum. 90 (2) (2019), 024905.
[56] A. Jeżowski, B.A. Danilchenko, M. Boćkowski, I. Grzegory, S. Krukowski, T. Suski, T. Paszkiewicz, Thermal conductivity of GaN crystals in 4.2–300 K range, Solid State Commun. 128 (2) (2003) 69–73.
[57] C. Mion, J.F. Muth, E.A. Preble, D. Hanser, Accurate dependence of gallium nitride thermal conductivity on dislocation density, Appl. Phys. Lett. 89 (9) (2006).
[58] R.B. Simon, J. Anaya, M. Kuball, Thermal conductivity of bulk GaN—Effects of oxygen, magnesium doping, and strain field compensation, Appl. Phys. Lett. 105 (20) (2014), 202105.
[59] R. Rounds, B. Sarkar, T. Sochacki, M. Bockowski, M. Imanishi, Y. Mori, R. Kirste, R. Collazo, Z. Sitar, Thermal conductivity of GaN single crystals: influence of impurities incorporated in different growth processes, J. Appl. Phys. 124 (10) (2018), 105106.
[60] Q. Zheng, C. Li, A. Rai, J.H. Leach, D.A. Broido, D.G. Cahill, Thermal conductivity of GaN, ^{71}GaN, and SiC from 150 K to 850 K, Phys. Rev. Materials 3 (1) (2019), 014601.
[61] H. Li, R. Hanus, C.A. Polanco, A. Zeidler, G. Koblmüller, Y.K. Koh, L. Lindsay, GaN thermal transport limited by the interplay of dislocations and size effects, Phys. Rev. B 102 (1) (2020), 014313.

[62] R. Rounds, B. Sarkar, D. Alden, Q. Guo, A. Klump, C. Hartmann, T. Nagashima, R. Kirste, A. Franke, M. Bickermann, Y. Kumagai, Z. Sitar, R. Collazo, The influence of point defects on the thermal conductivity of AlN crystals, J. Appl. Phys. 123 (18) (2018), 185107.
[63] R.L. Xu, M. Muñoz Rojo, S.M. Islam, A. Sood, B. Vareskic, A. Katre, N. Mingo, K. E. Goodson, H.G. Xing, D. Jena, E. Pop, Thermal conductivity of crystalline AlN and the influence of atomic-scale defects, J. Appl. Phys. 126 (18) (2019), 185105.
[64] Z. Cheng, Y.R. Koh, A. Mamun, J. Shi, T. Bai, K. Huynh, L. Yates, Z. Liu, R. Li, E. Lee, M.E. Liao, Y. Wang, H.M. Yu, M. Kushimoto, T. Luo, M.S. Goorsky, P. E. Hopkins, H. Amano, A. Khan, S. Graham, Experimental observation of high intrinsic thermal conductivity of AlN, Phys. Rev. Mater. 4 (4) (2020), 044602.
[65] G.A. Slack, R.A. Tanzilli, R.O. Pohl, J.W. Vandersande, The intrinsic thermal conductivity of AlN, J. Phys. Chem. Solids 48 (7) (1987) 641–647.
[66] A.V. Inyushkin, A.N. Taldenkov, D.A. Chernodubov, E.N. Mokhov, S.S. Nagalyuk, V.G. Ralchenko, A.A. Khomich, On the thermal conductivity of single crystal AlN, J. Appl. Phys. 127 (20) (2020).
[67] Y.B. Liu, J.Y. Yang, G.M. Xin, L.H. Liu, G. Csányi, B.Y. Cao, Machine learning interatomic potential developed for molecular simulations on thermal properties of β-Ga_2O_3, J. Chem. Phys. 153 (14) (2020), 144501.